The Effects of Numerical Dissipation on Hurricane Rapid Intensification with Observational Heating

M. B. Hasan[1], S. R. Guimond[2], M. L. Yu[1], S. Reddy[3], and F. X. Giraldo[3]

[1]Department of Mechanical Engineering, University of Maryland, Baltimore County, Baltimore, MD, USA
[2]Joint Center for Earth Systems Technology and Department of Physics, University of Maryland, Baltimore County, Baltimore, MD, USA
[3]Department of Applied Mathematics, Naval Postgraduate School, Monterey, CA, USA

Key Points:

- The WRF dynamic core dissipates $\sim 20\%$ more kinetic energy than NUMA for a dry vortex forced by four-dimensional latent heating observations.
- Values of the eddy diffusivity in WRF need to be reduced by $\sim 50\%$ from those in NUMA in order to produce a similar intensity time series.
- Budgets and sensitivity tests indicate that the low-order approximation of the pressure gradient is the source of the dissipation in WRF.

Corresponding author: M. B. Hasan, `mdbadrh1@umbc.edu`

Corresponding author: S. R. Guimond, `sguimond@umbc.edu`

Abstract

The computational fluid dynamics of hurricane rapid intensification (RI) is examined through idealized simulations using two codes: a community-based, finite-difference/split-explicit model (WRF) and a spectral-element/semi-implicit model (NUMA). The focus of the analysis is on the effects of implicit numerical dissipation (IND) in the energetics of the vortex response to heating, which embodies the fundamental dynamics in the hurricane RI process. The heating considered here is derived from observations: four-dimensional, fully nonlinear, latent heating/cooling rates calculated from airborne Doppler radar measurements collected in a hurricane undergoing RI. The results continue to show significant IND in WRF relative to NUMA with a reduction in various intensity metrics: (1) time-integrated, mean kinetic energy values in WRF are ∼20% lower than NUMA and (2) peak, localized wind speeds in WRF are ∼12m/s lower than NUMA. Values of the eddy diffusivity in WRF need to be reduced by ∼50% from those in NUMA to produce a similar intensity time series.

Kinetic energy budgets demonstrate that the pressure contribution is the main factor in the model differences with WRF producing smaller energy input to the vortex by ∼23%, on average. The low-order spatial discretization of the pressure gradient in WRF is implicated in the IND. In addition, the eddy transport term is found to have a largely positive impact on the vortex intensification with a mean contribution of ∼20%. Overall, these results have important implications for the research and operational forecasting communities that use WRF and WRF-like numerical models.

Plain Language Summary

The intensity of a hurricane is primarily a balance between energy production and dissipation from various physical processes. Numerical models calculate this energy balance by solving complicated equations that attempt to capture these physical processes. Previous research has shown that the methods used to solve these equations can introduce additional dissipation into the system that affects the prediction of the storm intensity. In this paper, we examine this "numerical dissipation" idea more closely by conducting carefully designed comparisons between the community numerical model (WRF) and an advanced, research model (NUMA). Using observational estimates of heating in clouds, which feed the production of energy, we find that the WRF model produces significantly more numerical dissipation relative to NUMA that results in a reduced intensity of the storm. Our analysis indicates that the reason for the anomalous numerical dissipation in WRF is due to how the pressure gradient is computed. These results can have potentially important consequences for operational forecasts, especially the rapid intensification process. For example, the under-prediction or low bias of rapid intensification forecasts may be partly due to excessive numerical dissipation.

1 Introduction

The record-breaking 2020 Atlantic hurricane season and recent storms that leveled the Florida panhandle in 2018 (Hurricane Michael) and submerged parts of Texas in 2017 (Hurricane Harvey) illustrate the devastating impacts of these systems, even in the modern era. Unfortunately, as the climate system continues to warm, recent research suggests that intense hurricanes will likely become more common, produce more flooding rainfall, and last longer even after landfall (Knutson et al., 2015, 2019; Li & Chakraborty, 2020). As a result, hurricanes will likely place increasing stress on many sectors of society for various countries across the globe.

Accurate forecasting of hurricane track, intensity, storm surge, and rainfall from dynamical models can mitigate losses by facilitating disaster preparations and evacua-

tions that can save lives and billions of dollars in damages. However, the operational prediction of hurricane intensity, especially rapid intensification (RI), has been mainly stagnant (Marks & Shay, 1998; Rappaport et al., 2009), with large forecast errors still present today (DeMaria et al., 2014). As described in DeMaria et al. (2014), none of the deterministic models had RI forecasting capability from 1991 to around 2015. There has been some ability to forecast RI with both dynamical and statistical models since 2015, however, a significant under-prediction or low bias in RI cases is still present today (DeMaria et al., 2021).

The increase of kinetic energy in hurricane intensification, as well as RI, is driven by the vortex response to heating in convective clouds (e.g., Shapiro & Willoughby, 1982), where the source of moist enthalpy flux comes from the thermodynamic disequilibrium between the ocean and atmosphere, (e.g., Emanuel, 1986). Dissipation of energy occurs most prominently in the boundary layer through surface friction and a hierarchy of turbulent eddies of various scales. However, new research has shown that the hurricane boundary layer is not purely dissipative and contains coherent turbulent structures that can "backscatter" energy to larger scales (Sroka & Guimond, 2021). In numerical models, dissipation of energy can also occur implicitly through the algorithms used to solve the fluid-flow equations ("implicit numerical dissipation") or explicitly through the addition of filters. Implicit numerical dissipation can occur from the use of low-order discretizations of the governing equations in both space and time. For example, the use of second-order or upwind-biased spatial discretizations of the advective terms can result in substantial numerical dissipation error when compared to high-order (e.g., fifth) or centered schemes (Hoffman & Frankel, 2001; Skamarock & Klemp, 2008)).

In general, minimal numerical dissipation is desired in highly nonlinear computational fluid dynamics problems, such as hurricanes, because errors incurred from excessive dissipation can quickly propagate through the system. Kravchenko and Moin (1997) examined numerical errors in spectral and finite difference codes as well as the effects of sub-grid scale models in turbulent channel flow. They demonstrated that the high wavenumber portion of the energy spectrum is severely damped by truncation errors in low-order (e.g., second) finite-difference schemes, and the contribution of the sub-grid scale model is small in this context. By increasing the order of the finite-difference approximations, the results of their large eddy simulations and the performance of the sub-grid scale model were enhanced. Larsson et al. (2007) found that maintaining low numerical dissipation was important for simulating shock/turbulence interactions, especially for coarse resolution simulations where the fields are under-resolved and a sub-grid model is required (this is also the case in mesoscale atmospheric modeling). In these under-resolved simulations, the numerical dissipation was large enough to dampen or erase the smaller-scale motions on the grid and from the sub-grid model.

Continuous Galerkin (CG) and discontinuous Galerkin (DG) numerical methods have several unique properties which distinguish them from low-order (i.e., the order of accuracy equal to or smaller than two) methods and other high-order methods, such as finite volume/difference schemes. These include: 1) possessing low dissipation and dispersion errors for turbulent flows with highly disparate spatial and time scales; 2) achieving arbitrary high-order discretization for all spatial derivatives; and 3) highly scalable, and efficient on massively parallel supercomputers, such as those accelerated by Graphics Processing Units (GPUs) (Abdi et al., 2017, 2019). These superior numerical properties make high-order CG and DG methods attractive for hurricane research. The advantages of high-order numerical methods over their low-order counterparts for low Reynolds number flow problems has been demonstrated through a workshop series, The International Workshop on High-Order CFD Methods (Wang et al., 2013). However, when simulating under-resolved problems that require a sub-grid turbulence model and problems with discontinuities, high-order numerical schemes can have issues with excessive grid scale noise, aliasing and stability (Honein & Moin, 2004; Gassner & Beck, 2013; Moura

et al., 2017). These issues can lead to errors in the simulated flow or a failure of the simulation. To address these potential problems, de-aliasing techniques (Blaisdell et al., 1996; Gassner, 2013; Karamanos & Karniadakis, 2000; Fischer & Mullen, 2001; Gassner & Beck, 2013), localized artificial viscosity (Persson & Peraire, 2006; Yu et al., 2015) and limiters (Cockburn & Shu, 1998; Qiu & Shu, 2005; Zhang & Shu, 2010) can be used to stabilize flow simulations. In this study, we rely on a combined approach that applies artificial viscosity based on output from a turbulent kinetic energy (TKE) sub-grid model for turbulent diffusion; see details in Section 2.3.

Takemi and Rotunno (2003) studied the effects of sub-grid mixing and numerical filtering in squall line simulations using the Weather Research and Forecasting (WRF) model, which is a finite difference based code that can provide high order discretization for the advective (or flux divergence) terms only (Skamarock & Klemp, 2008). The authors found that using a fifth-order, upwind-biased advection scheme along with a standard TKE sub-grid model resulted in many noisy, grid-scale convective cells. Rather than applying an explicit numerical filter, which could damage the physical modes, the authors tuned the TKE sub-grid model coefficient to produce reasonable convective structures and energy scaling with wavelength. They also tested the inclusion of an explicit numerical filter and found that it had a much larger effect on the solutions than the sub-grid TKE model, which highlights the importance of analyzing numerical dissipation. It is clear that in order to ensure both high accuracy and stability of a simulated flow, a careful balance between signal and noise must be achieved.

In a theoretical hurricane study, Guimond et al. (2016) showed that the vortex response to simple, impulsive, asymmetric thermal anomalies can produce significant differences in system intensity across models due to the amount of implicit numerical dissipation. The community atmospheric model (WRF) was shown to have anomalously large implicit numerical dissipation when compared to research atmospheric codes [the High-Gradient (HIGRAD) model and the Non-hydrostatic Unified Model of the Atmosphere (NUMA)], which resulted in a muted intensity response from asymmetric thermal anomalies. The HIGRAD and NUMA models produced a more energetic response due to much less numerical dissipation. Spectral kinetic energy budgets showed that the pressure gradient term was the dominant source of the anomalous dissipation in WRF with the flux of inertia-gravity wave energy describing most of the variance in the pressure term. Acoustic and inertia-gravity waves are considered fast modes in the equation set, which are split off from the slow modes in WRF. This understanding lead to the recommendation that the time integration scheme was the main culprit for the numerical dissipation in WRF. Evidence for this hypothesis was shown through sensitivity tests with different time integration schemes in NUMA, which showed significant differences in the amount of energy and role of the pressure term.

In this work, we study the response of a tropical storm-like vortex to time-dependent, 3-D observational heating calculated from airborne Doppler radar measurements in the RI of Hurricane Guillermo (1997). The remainder of the paper is organized as follows. In Section 2, a detailed description of the numerical models and simulation setup is presented. Therein, we introduce the WRF and NUMA models, vortex initialization and heating strategies, and eddy viscosity and diffusivity setup. Comparison of the wind field features, e.g., maximum and azimuthal mean wind speed as well as kinetic energy, from WRF and NUMA is discussed in Section 3. In this section, we also present kinetic energy budget analyses to explain the wind field disparity between WRF and NUMA. Important implications of this work in the hurricane research and operational fields are given in Section 4. Future work is also discussed in this section.

2 Description and setup of numerical models

A comprehensive introduction of the governing equations and numerical methods used in the WRF-ARW (hereafter WRF) and NUMA models have been given in Guimond et al. (2016). For completeness, we briefly review them below.

2.1 The WRF Model

The WRF model solves the compressible, non-hydrostatic Euler equations in a conservative form with a η mass vertical coordinate (Laprise, 1992; Skamarock & Klemp, 2008). For comparisons with NUMA, all variables are interpolated to regular height levels in post-processing. Note that the differences between the η levels and height are very small for these idealized simulations. The simplified model equations for a dry atmosphere can be expressed as follows, using a Laplacian operator for explicit diffusion and η as the vertical coordinate:

$$\frac{\partial mu}{\partial t} + \nabla \cdot (m\mathbf{u}u) = -\frac{m}{\rho}\frac{\partial \hat{p}}{\partial x} + fmv + \nabla \cdot (m\mu\nabla u) \tag{1}$$

$$\frac{\partial mv}{\partial t} + \nabla \cdot (m\mathbf{u}v) = -\frac{m}{\rho}\frac{\partial \hat{p}}{\partial y} - f\mu u + \nabla \cdot (m\mu\nabla v) \tag{2}$$

$$\frac{\partial mw}{\partial t} + \nabla \cdot (m\mathbf{u}w) = g\left(\frac{\partial \hat{p}}{\partial \eta} - \hat{m}\right) + \nabla \cdot (m\mu\nabla w) \tag{3}$$

$$\frac{\partial m\theta}{\partial t} + \nabla \cdot (m\mathbf{u}\theta) = S + \nabla \cdot \left(m\kappa\nabla\hat{\theta}\right) \tag{4}$$

$$\frac{\partial m}{\partial t} + \nabla \cdot (m\mathbf{u}) = 0. \tag{5}$$

Here u, v and w are the velocities in three dimensions, $m = m(x, y)$ is the mass per unit area within a column, θ is the potential temperature, ρ is the dry air density, $\hat{p}$ is the perturbation pressure, f is the Coriolis parameter, g is gravity, μ is the eddy viscosity, κ is the thermal diffusivity, S is the heating rate source term, and ∇ is the three-dimensional gradient operator. Variables with a hat denote perturbations from the hydrostatically balanced reference state.

A combined finite-difference/finite-volume spatial discretization of the governing equations is employed in WRF. In the horizontal and vertical directions, a spatially staggered Arakawa C grid is utilized where velocities are defined on the cell faces and scalars at the cell centers. For the nonlinear advective terms, a fifth-order, upwind-biased discretization in the horizontal and a third-order scheme in the vertical are typically used. We have utilized these settings here, but also tested the impacts of the less diffusive, even-ordered schemes (sixth-order and fourth-order in the horizontal and vertical dimensions, respectively). The differences between the even-ordered and odd-ordered schemes were small (maximum values of +/- 0.5 m/s in the eyewall) and therefore, we utilize the odd-ordered formulations in all presented results. The WRF model relies on a split-explicit time integration process, where acoustic and gravity wave modes are calculated using a small time step and advection is computed on a larger time step (Klemp & Wilhelmson, 1978; Wicker & Skamarock, 2002; Skamarock & Klemp, 2008). Horizontal modes are solved explicitly within the small time stage, while vertical modes are implicitly solved. The implicit solve is done with backward Euler. A third-order Runge-Kutta scheme is used to perform the overall time integration, including both the small- and large-time step equations. The small time step results are applied as a correction to the large time step calculations during the Runge-Kutta time integration. More details on WRF can be found in (Skamarock & Klemp, 2008). Finally, we seek to produce minimally dissipative WRF solutions and therefore, we have turned *off* all filtering/damping options:

explicit sixth-order numerical filtering, vertical velocity damping, divergence damping and external mode damping. Artificial viscosity is applied at the model top and through the Laplacian operators in the above equations are discussed further in Section 2.3.

2.2 The NUMA Model

The NUMA model is capable of using various forms of the Euler equations [e.g., Giraldo and Restelli (2008), Giraldo et al. (2010)]. However, for this study, we use the non-conservative form using potential temperature as the thermodynamic variable [Kelly and Giraldo (2012), Giraldo et al. (2013)] to be consistent with Guimond et al. (2016). The choice of conservative or non-conservative equation set is not expected to make a significant difference because the error resulting from the non-conservative set is much lower than the temporal error (Giraldo & Restelli, 2008). Instead of the η mass vertical coordinate, physical height z is used in NUMA. The governing equations are expressed as:

$$\frac{\partial u}{\partial t} + \mathbf{u} \cdot \nabla u = -\frac{1}{\rho}\frac{\partial \hat{p}}{\partial x} + fv + \nabla \cdot (\mu \nabla u) \tag{6}$$

$$\frac{\partial v}{\partial t} + \mathbf{u} \cdot \nabla v = -\frac{1}{\rho}\frac{\partial \hat{p}}{\partial y} - fu + \nabla \cdot (\mu \nabla v) \tag{7}$$

$$\frac{\partial w}{\partial t} + \mathbf{u} \cdot \nabla w = -\frac{1}{\rho}\frac{\partial \hat{p}}{\partial z} - \frac{\hat{\rho}}{\rho} g + \nabla \cdot (\mu \nabla w) \tag{8}$$

$$\frac{\partial \theta}{\partial t} + \mathbf{u} \cdot \nabla \theta = S + \nabla \cdot \left(\kappa \nabla \hat{\theta}\right) \tag{9}$$

$$\frac{\partial \rho}{\partial t} + \nabla \cdot (\rho \mathbf{u}) = 0 \tag{10}$$

The spatial discretization of Eqs. (6)-(10) is carried out using the CG spectral element method (CG-SEM) (Giraldo & Restelli, 2008; Giraldo et al., 2013; Giraldo, 2020). Specifically, the physical domain is decomposed into a set of non-overlapping hexahedral elements and inside each element, the state variables are represented by polynomial expansion using Lagrange basis functions of a chosen order. The continuous spatial derivatives are constructed in discrete form by analytically taking derivatives of the polynomials that approximate the solutions. The state variables in each element are collocated with each other and placed at unequally spaced Legendre-Gauss-Lobatto points. In this study, we utilize fifth-order polynomial basis functions in all three spatial dimensions, which also provides fifth-order accuracy for all spatial derivatives and is identical to that presented in Guimond et al. (2016). Note that the stencil for all polynomial orders in NUMA is symmetric about the element centroid, so upwind-biased diffusion for fifth-order polynomials is not present. For time integration, the three-dimensional semi-implicit methodology (Giraldo et al., 2013) is used along with a second-order leapfrog scheme (LF2). A first-order Robert-Asselin time filter is applied to stabilize the LF2 scheme. The above description of NUMA comprises our control simulations. Several other time integration formulations are available in NUMA and we will note where sensitivity tests have been conducted. Interested readers are referred to Giraldo and Restelli (2008); Giraldo et al. (2013) for more details of the NUMA model.

2.3 Details of Simulation Setup

Careful analysis has been undertaken to setup WRF and NUMA nearly exactly the same to isolate any differences in the model solutions to the numerical schemes that comprise the dynamic core. The computational domain is a box extending 800 km in the horizontal directions and 20 km in the vertical direction. In WRF, 2 km grid spacing

in the horizontal is chosen to match that of the radar observations used as forcing and to be consistent with Guimond et al. (2016). The first model level is found at 167 m with constant vertical spacing of 333 m up to the model top (60 levels). To match the horizontal and vertical grid spacing in WRF, we have used 80 elements in each horizontal direction and 12 elements in the vertical direction along with fifth-order polynomials in all dimensions for the NUMA grid, as described in Section 2.2. These settings yield an element-averaged grid spacing in NUMA of ~ 2 km in the horizontal and ~ 333 m in the vertical. A time step of 2 seconds is used in each model.

Periodic boundary conditions are used in both horizontal directions in each model. A gravity wave absorbing zone (sine-squared function) is imposed at the top of the computational domain with the WRF zone occupying the top 4 km along with a small coefficient (0.00833) and the NUMA zone representing the top 1 km with a large coefficient (1.0). The differences in the absorbing zones are due to stability issues and sensitivity tests show the results are not sensitive to these choices. The free-slip boundary condition is applied at the bottom of the computational domain in each model, which disables fluxes of quantities (such as heat) from the surface and prevents a frictional boundary layer from developing. These idealizations enable the focus to be on the vortex dynamic response to the imposed heating. The simulations are run without moisture, but instead, four-dimensional latent heating/cooling rates derived from airborne Doppler radar observations are used to force the model as described below.

In post-processing, both WRF and NUMA fields are interpolated to a uniform, collocated grid at the horizontal/vertical grid spacings listed above. Linear interpolation is used to post-process the WRF results. To post-process NUMA results, a high-order interpolation based on Lagrange polynomials is applied, which is facilitated by the spectral element method (since by construction the solution exists everywhere in the element). To ease interpolation, any hexahedral element in the physical space (x, y, z) can be transformed into a standardized space $(\alpha, \beta, \gamma) \in [-1, 1] \times [-1, 1] \times [-1, 1]$. Thus, for any Nth-order standard hexahedral element, there are N+1 Legendre-Gauss-Lobatto points, namely, $(\alpha_i, \beta_i, \gamma_i)$, $i = 1, \ldots, N{+}1$, in each direction α, β and γ. The Lagrange polynomial basis $L_{IJK}(\alpha, \beta, \gamma)$, $I, J, K = 1, \ldots, N + 1$, can be constructed using the tensor product as

$$L_{IJK}(\alpha,\beta,\gamma) = \left(\prod_{i=1,i\neq I}^{N+1} \frac{\alpha-\alpha_i}{\alpha_I-\alpha_i}\right)\left(\prod_{j=1,j\neq J}^{N+1} \frac{\beta-\beta_j}{\beta_J-\beta_j}\right)\left(\prod_{k=1,k\neq K}^{N+1} \frac{\gamma-\gamma_k}{\gamma_K-\gamma_k}\right). \tag{11}$$

Then, any value of the flow variables $V(\alpha, \beta, \gamma)$, such as the wind speed, inside a hexahedral element can be interpolated from the solutions V_{IJK}, $I, J, K = 1, \ldots, N{+}1$, on the Legendre-Gauss-Lobatto points as

$$V(\alpha,\beta,\gamma) = \sum_{I=1}^{N+1}\sum_{J=1}^{N+1}\sum_{K=1}^{N+1} L_{IJK}(\alpha,\beta,\gamma)V_{IJK}. \tag{12}$$

The initial conditions are identical in each model. The hydrostatic and gradient-wind balanced, tropical storm-like vortex with axisymmetric tangential winds described in Eq. (10) of Guimond et al. (2016) is utilized here, which is similar to the study of Nolan and Grasso (2003). The tangential velocity field in the radius–height plane for this initial vortex is shown in Fig. 1. On top of this vortex, four-dimensional latent heating/cooling rates derived from airborne Doppler radar measurements in rapidly intensifying Hurricane Guillermo (1997) described in Guimond et al. (2011), are added as a source term in the potential temperature equation in both WRF and NUMA. These heating fields

are computed on a grid covering the inner-core of the system out to a radius of ~ 60 km with a grid spacing of 2 km and 0.5 km in the horizontal and vertical dimensions, respectively. There are ten heating snapshots covering ~ 5.7 h with a time step of ~ 34 minutes. The peak heating is located at a radius of 25 - 30 km, which is well inside the radius of maximum wind (RMW) of the initial vortex (~ 50 km). This heating and vortex configuration represents the rapid intensification process well, where convective bursts are the main driving force, e.g., (M. Montgomery et al., 2006; Reasor et al., 2009; Guimond et al., 2010; Rogers et al., 2013). Guimond et al. (2011) conducted an extensive uncertainty analysis of the latent heat retrievals and found they were reasonably accurate, especially for convective bursts with randomly distributed errors in the heating magnitudes of $\sim 16\%$ for updrafts greater than 5 m/s. In addition, Guimond and Reisner (2012) inserted the heating retrievals into realistic forecasts of Guillermo and found very good agreement in the predicted wind fields relative to observations.

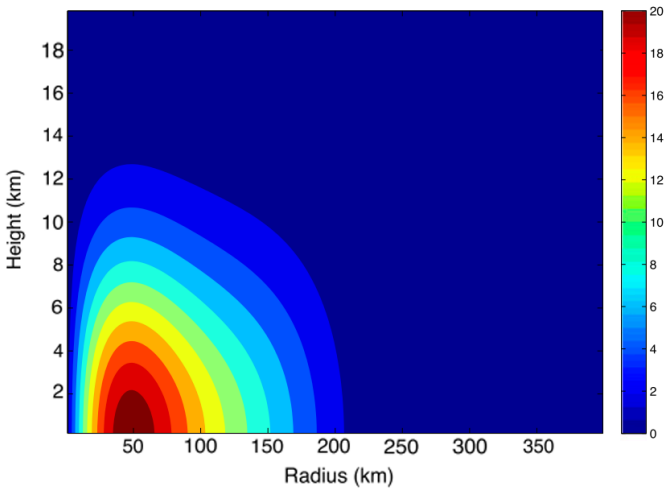

Figure 1: Axisymmetric tangential velocity (m/s) in the radius-height plane for the initial vortex used in each model.

Starting from the initial conditions, the first heating snapshot is introduced into the model over a 30 minute period using a hyperbolic tangent function. Then, the remaining heating snapshots are linearly interpolated to the next observation time over a 34 minute period. After the last observation time, the heating is kept constant up to 6 hours, which is the end of our simulations. Fig. 2 shows the three-dimensional structure of the heating for three snapshots and the time evolution function used to control the forcing in the models. Note that we have also added an exponentially decaying function at the upper-edge of the observational domain (10 km) to smoothly transition the data into the model grid, which helps maintain numerical stability.

Both models are also supplied the same explicit diffusion settings. While we can utilize the same sub-grid scale turbulence scheme in WRF and NUMA for our comparisons, the differences in the dynamic core of each model and associated dissipation characteristics will likely produce different eddy viscosity values during the course of the simulations. To isolate the model differences to the numerical formulation, we developed a simple height-dependent eddy viscosity model based on output from the WRF 3D turbulent kinetic energy (TKE) sub-grid turbulence scheme. Initially, we conducted a WRF simulation with the 3D TKE scheme to get an idea of the eddy viscosity and diffusiv-

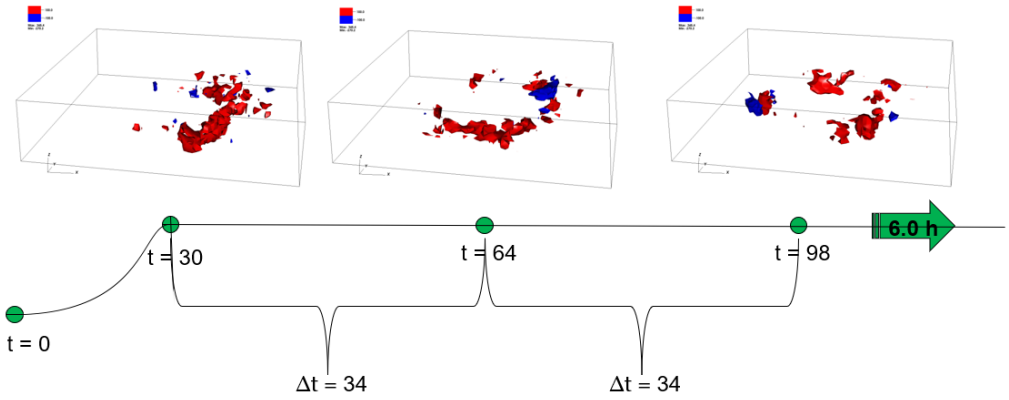

Figure 2: Three-dimensional isosurfaces of latent heating (red; 100 K/h) and cooling (blue; -100 K/h) retrieved from airborne Doppler measurements in rapidly intensifying Hurricane Guillermo (1997). Three example snapshots of this heating are shown with the storm-centered volume extending 120 km on a side in the horizontal and 20 km in the vertical. The time evolution function used to force the heating into the model is also shown with units of minutes, unless noted otherwise.

ity values produced from the vortex and heating. Following a parcel, the sources and sinks of TKE in this scheme depend on the shear, buoyancy and dissipation. Details describing the implementation of this scheme in WRF, including the parameterization for dissipation, can found in Skamarock et al. (2021). The observational heat forcing will generate TKE from both the buoyancy and shear terms, but we only focus on the output eddy viscosities and diffusivities, which are calculated as

$$K_{h,v} = C_k l_{h,v} \sqrt{e} \tag{13}$$

where e is the TKE, C_k is a constant of 0.15, and l is a length scale, which is around 2000 m in the horizontal and 375 m in the vertical. Figure 3 shows plots of the horizontal eddy viscosity from the 3D TKE scheme at 0.50 km and 9.80 km height at 6 h . The eyewall is visible in the figures with viscosity values of ~ 240 $m^2 s^{-1}$ or larger in a thin ring at 0.5 km height and a broader region of $500 - 750$ $m^2 s^{-1}$ values at 9.80 km height.

Localized regions of higher viscosity values near 400 $m^2 s^{-1}$ and 1500 $m^2 s^{-1}$ at lower and upper levels, respectively, are connected to large, vertically coherent heating pulses from convective bursts. Note that we have set the turbulent Prandtl number in WRF, which has a default value of 1/3, to 1 which enables the same eddy viscosity/diffusivity values for momentum and scalars. There are areas of the WRF software where the default value is hard coded and we have taken careful steps to maintain values of 1 throughout the code. The turbulent Prandtl number is set to 1 in NUMA as well.

Fig. 4 shows the maximum horizontal and vertical eddy viscosity values produced over the 6 h WRF simulation as a function of height. Both curves have relatively small values at lower levels, but they increase sharply at middle levels with some additional oscillations up to ~ 16 km height. The large values found at middle to upper levels are from the strong heating pulses associated with convective bursts as seen in Fig. 3. The values drop off sharply at ~ 16 km height because that is where the gravity wave sponge is introduced into the model. The maximum horizontal viscosity values are about five

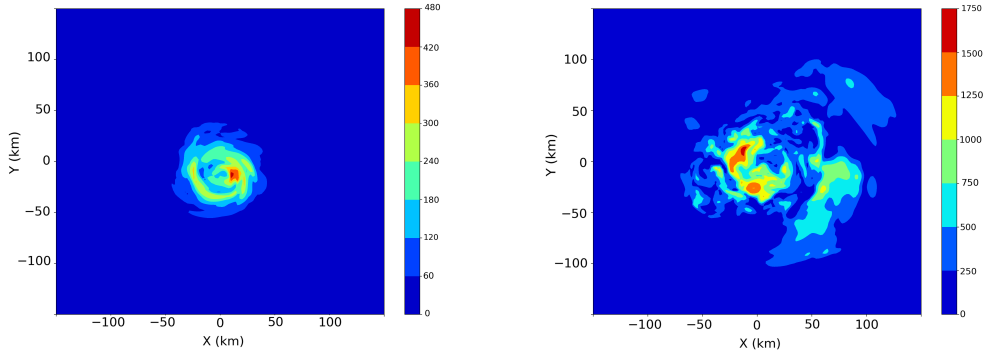

Figure 3: Eddy viscosity values output from the WRF 3D TKE scheme at 6 h and 0.5 km height (left panel) and 9.8 km height (right panel).

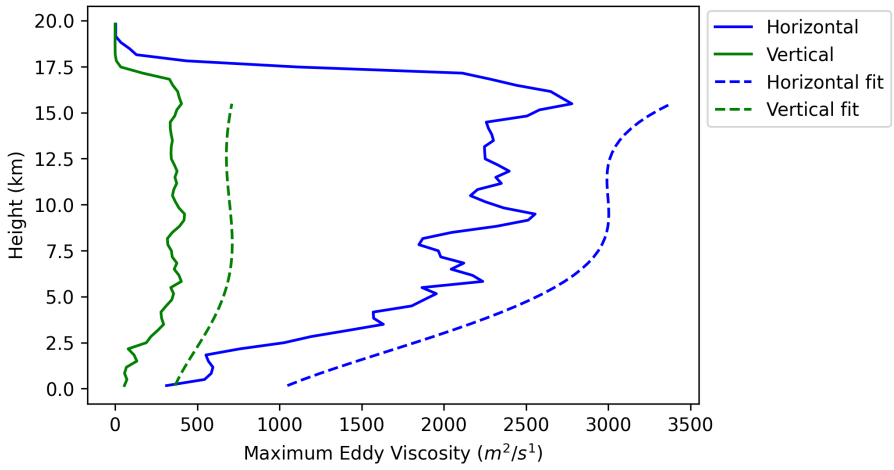

Figure 4: Maximum eddy viscosity values from the 3D TKE scheme in WRF as a function of height. The maximum values are taken over the 6 h simulation.

times larger than the vertical values. Overlaid on top of the maximum viscosity curves are high-order polynomial fits that approximate the general structure and values of the eddy viscosity data. These fits take the following form

$$visc(z) = \tilde{a}z^5 + \tilde{b}z^4 + \tilde{c}z^3 + \tilde{d}z^2 + \tilde{e}z + \tilde{f} \tag{14}$$

where z is the geometric height in meters and the coefficients of the fifth-order polynomial are found in Table 1. To stabilize the NUMA code, an extra constant was added to the $\tilde{f}$ coefficient for both the horizontal and vertical polynomial fits. The $\tilde{f}$ coefficient is shown in Table 1 and the curves in Fig. 4 include this offset. Finally, these height-dependent eddy viscosity values are used in *both* WRF and NUMA for momentum and scalar diffusion in the comparison simulations. This simple explicit diffusion model is intended to both stabilize each numerical model and also represent, to some degree, realistic subgrid scale turbulent diffusion from the TKE scheme.

Table 1: Coefficients for the horizontal and vertical viscosity polynomial fits. Both WRF and NUMA use the exact same values.

Coefficients	$\tilde{a}$	$\tilde{b}$	$\tilde{c}$	$\tilde{d}$	$\tilde{e}$	$\tilde{f}$
Horizontal	-0.012760	0.6946	-11.57	53.28	255.90	1003.90
Vertical	-0.004572	0.2150	-3.29	15.05	43.16	357.65

3 Results

3.1 Time Series and Windspeed Structure

In this section, we compare the solutions from the WRF and NUMA control simulations in terms of time series of horizontal wind speed and kinetic energy as well as the structure of windspeed perturbations. Here, perturbation is defined as the total wind speed at a particular time minus the wind speed of the initial condition, which helps identify the wind structures produced from the observational heating.

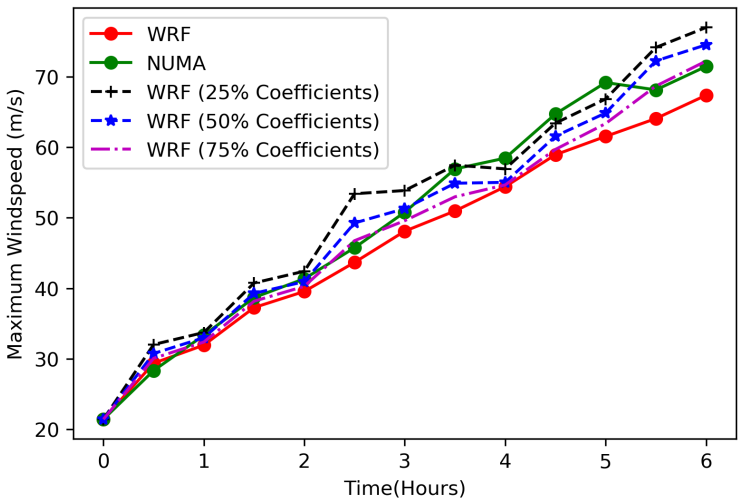

Figure 5: Time series of maximum windspeed for the control WRF and NUMA simulations. The dashed lines show WRF sensitivity tests where the eddy viscosity values were set to a certain percentage of the default values.

Fig. 5 shows the maximum windspeed output every 30 minutes for the control WRF and NUMA simulations with solid red and green lines, respectively. The maximum winds increased by about 45 m/s in 6 h, which is a very large RI rate. The reason for this high rate, besides the idealized setup, is the much larger (and weaker) initial vortex compared to that which occurred in nature, which drives a large inward movement of angular momentum and associated increase in winds. Guimond and Reisner (2012) considered the same observational heating as the present study, but used an initial vortex based on radar observations of Hurricane Guillermo (1997) that had a much smaller RMW ($\sim$ 30 km) compared to the vortex used here ($\sim$ 50 km). Guimond and Reisner (2012) found that the minimum pressure dropped by about 12 - 15 hPa in 6 h with the realistic initial vortex, which compared more favorably with observations than the present vortex. Never-

theless, the goal of this study is to analyze the idealized vortex response to heating pulses derived from observations in a RI system and examine the effects of implicit numerical dissipation in this process. We do not intend to simulate and reproduce the Guillermo case study. Thus, the current initial vortex and model setup are sufficient for the goals of this work.

Fig. 5 also shows that after $\sim 2\ h$, the NUMA winds begin to increase relative to WRF and during the last couple of hours of the simulations, the maximum windspeed is 2 - 7 m/s or 4 - 12% higher in NUMA compared to WRF. In an attempt to more closely match the time series of WRF and NUMA, three sensitivity tests were conducted with WRF where the eddy viscosity values were set to 25%, 50% and 75% of the default values. The 75% tests still show significantly reduced maximum winds relative to NUMA, while the 25% tests generally seem too high, especially before 3.5 h. In general, the 50% tests show a much closer match to NUMA, especially up to and including 3.5 h, despite the anomalously high value at 2.5 h. There is some larger variability between 4 - 6 h, but smoothing through that variability indicates a reasonable match to NUMA. Therefore, these results indicate that in order to produce a similar intensity time series to NUMA, the explicit diffusion in WRF must be turned down significantly, with a reduction in eddy viscosity values of $\sim 50\%$ relative to those in NUMA.

Additional time series diagnostics for azimuthal mean quantities were also calculated. While the environment surrounding the vortex has no mean flow, the observational heat forcing has an azimuthal wavenumber-one structure as can be seen in Fig. 2, which produces a wavenumber-one flow asymmetry that slowly moves the vortex to the southeast. The storm center is computed through a simple iterative method that finds the position which maximizes the azimuthal mean windspeed. The data are interpolated onto a cylindrical grid with this storm center and the azimuthal mean quantities are calculated.

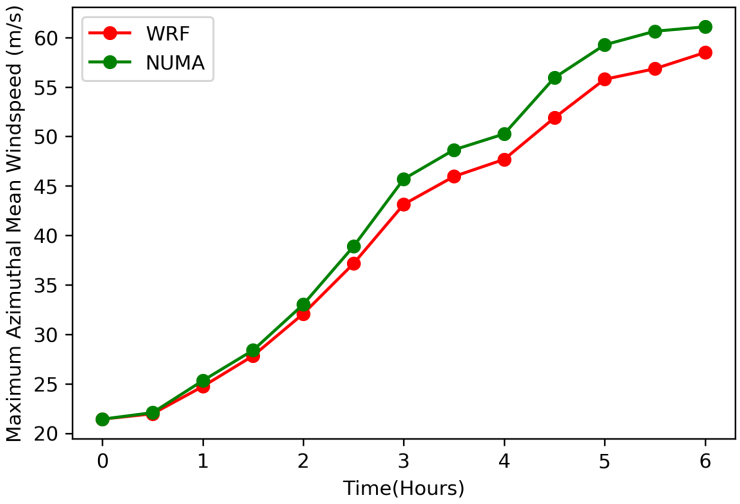

Figure 6: Time series of maximum azimuthal mean windspeed for the control WRF and NUMA simulations.

Figs. 6 and 7 show the times series of azimuthal mean windspeed and mean kinetic energy, respectively. These figures show a similar qualitative pattern as the maximum windspeed with NUMA producing larger mean windspeeds and kinetic energy values relative to WRF, with those differences growing over time. In the last couple of hours, the

maximum azimuthal mean windspeed is about 4 m/s or 8% higher in NUMA compared to WRF. The mean kinetic energy follows a very similar pattern to the windspeed and will be used as a reference for a dynamical budget analysis, presented in Section 3.2, to explain the reasons behind the model differences. While the differences between WRF and NUMA are not large for these mean quantities, there is more substantial variability on local space and time scales, which is demonstrated next. In addition, it is important to keep in mind the short time period of these simulations (dictated by the available observations) and the idealized nature of the setup, both of which will limit the variability in the models.

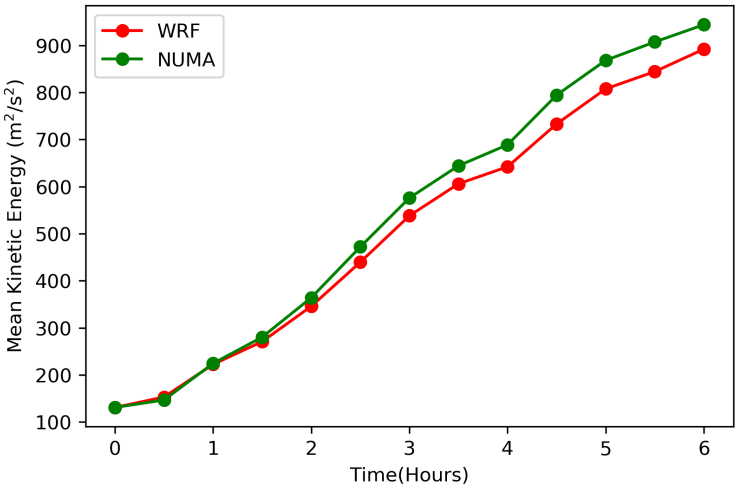

Figure 7: Time series of azimuthal mean kinetic energy averaged over the eyewall ($\sim$ 10 - 50 km radius) and height ($\sim$ 0.19 - 1.5 km) for the control WRF and NUMA simulations.

Snapshots of perturbation wind speed in WRF and NUMA are shown for the 4, 5 and 6 hour time periods in Figs. 8 and 9. At 4 h and 0.19 km height in Fig. 8, the perturbation windspeed shows a tight inner-core in both models with the windspeed maximum occurring in the North or North-East section of the vortex, reflecting the asymmetric heating input. The NUMA windspeeds are visibly larger than WRF by about 5 m/s averaged over the eyewall region with peak differences of 6 - 7 m/s in localized regions, such as the larger band in the Eastern eyewall. The majority of the model differences are concentrated in the center part of the eyewall, but there are also also regions of positive differences in some banded structures to the North and North-East of the center. The low wind region in the eye is larger in NUMA when compared to WRF, which creates a larger radial windspeed gradient when accounting for the larger values in the eyewall. Outside of the strongest winds in the eyewall and a few banded areas, the model differences are smaller with some regions positive and other regions negative. At higher levels (4.83 km height) in Fig. 8, the model differences are smaller with peak positive values of 4 - 5 m/s in smaller regions. More significant negative values (WRF winds stronger than NUMA) are occurring at the eye-eyewall interface and also indicate stronger radial gradients as found at lower levels.

At 5 h and 6 h, the vortex has reached peak intensity with perturbation windspeeds of $\sim$ 60 m/s found on the Northeast and Northern side of the storm as shown in Fig. 9. At these time periods, the RMW of the vortex is 15 - 20 km with NUMA on the lower side and WRF on the higher side of that interval. The RMW of the initial vortex was $\sim$ 50 km and this large, rapid contraction rate is consistent with the rapid increase in winds from conservation of angular momentum.

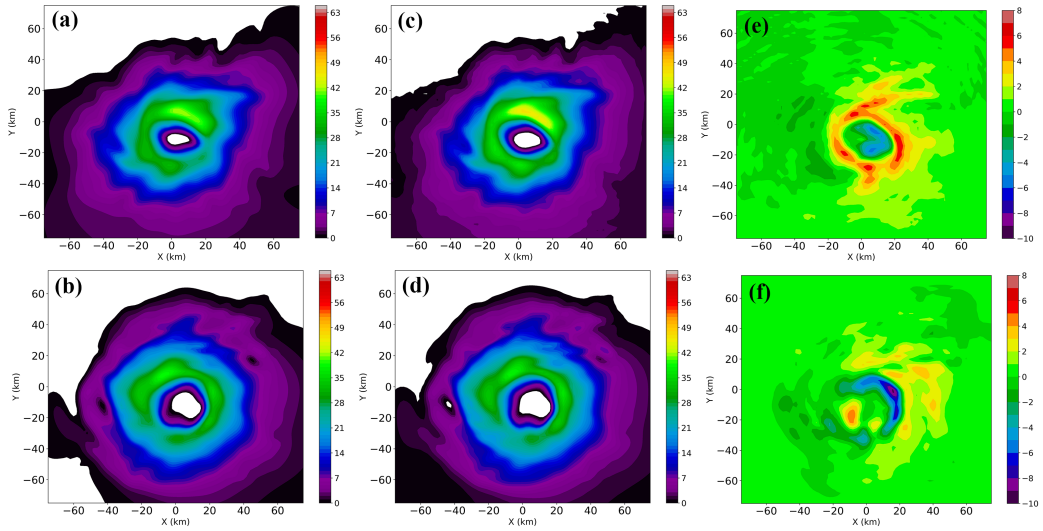

Figure 8: Horizontal wind speed perturbations and differences at 4 h for WRF and NUMA. Panels (a) and (b) show results from WRF at 0.19 km and 4.83 km heights, respectively, while panels (c) and (d) show results from NUMA at the same levels. Panels (e) and (f) show the differences (NUMA - WRF) at the same heights.

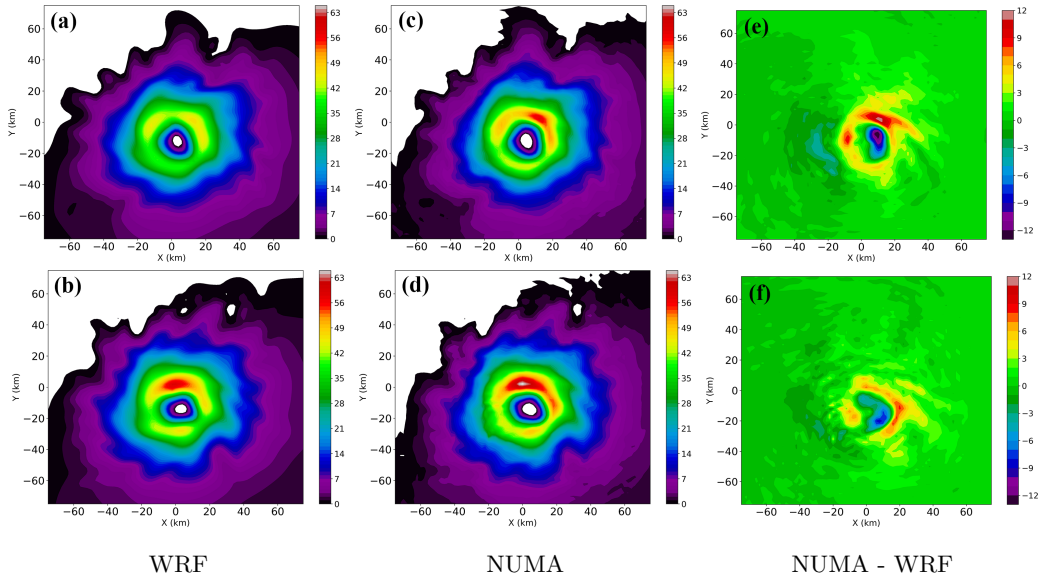

Figure 9: The same as in Fig. 8, only showing the 0.19 km height level at 5 h and 6 h in WRF in panels (a) and (b), respectively and NUMA in panels (c) and (d). Panels (e) and (f) show the differences (NUMA - WRF) at the same corresponding time periods.

At 5 h, NUMA shows significantly stronger winds than WRF by 7 - 8 m/s within large portions of the northern eyewall including peak differences of up to +12 m/s. Similar to the previous time period, the low-wind eye of NUMA is a bit wider than WRF, which produces large negative differences in the eye and a larger radial wind gradient. Some thin bands of higher wind differences can also be seen to the North and Northeast of the storm, which may be related to vortex Rossby wave dynamics. At 6 h, the local wind differences are smaller, but still significant in that much of the eyewall has positive differences of $\sim$ 5 m/s with larger values on the Eastern side of the vortex.

3.2 Budget Analyses

The previous section established clear differences between the two numerical models with NUMA producing a larger intensity response. How can this be given that each model was set up exactly the same with the same initial conditions and same heat forcing? The answer to this question lies in the design of the numerical schemes that make up the dynamic core of each model and in this section, we analyze how the intensity differences are produced and highlight parts of the numerical scheme that are driving this effect.

The horizontal kinetic energy for the azimuthal mean vortex in cylindrical coordinates (r,θ,z) is expressed as

$$\bar{K} = \frac{1}{2}(\bar{u}^2 + \bar{v}^2) \tag{15}$$

where u is the radial windspeed, v is the tangential windspeed and the overbar indicates an azimuthal mean quantity. After azimuthally averaging, these variables and those below are functions of radius (r) and height (z) unless noted otherwise. After multiplying the radial and tangential equations of motion by their corresponding velocity, summing the two equations and applying Reynolds decomposition in the azimuthal direction (the over bar and prime notations below indicate azimuthal mean and eddy variables, respectively), we arrive at the transport equation for azimuthal mean kinetic energy,

$$\frac{\partial \bar{K}}{\partial t} = M + E + P + D \tag{16}$$

where,

$$M = -\left(\frac{1}{r}\frac{\partial}{\partial r}(\bar{u}\bar{K}r) + \frac{1}{\bar{\rho}}\frac{\partial}{\partial z}(\bar{w}\bar{K}\bar{\rho})\right),$$

$$E = -\left(\frac{\bar{u}}{r}\frac{\partial}{\partial r}(\overline{u'u'}r) + \frac{\bar{u}}{\bar{\rho}}\frac{\partial}{\partial z}(\overline{u'w'}\bar{\rho}) + \frac{\bar{v}}{\bar{\rho}}\frac{\partial}{\partial z}(\overline{v'w'}\bar{\rho}) + \frac{\bar{v}}{r}\frac{\partial}{\partial r}(\overline{u'v'}r) - \frac{\bar{u}\overline{v'v'}}{r} + \frac{\bar{v}\overline{u'v'}}{r}\right),$$

$$P = -\frac{\bar{u}}{\bar{\rho}}\left(\frac{\partial \bar{p}}{\partial r}\right), \quad \text{and} \quad D = \left(\bar{u}\bar{D}_r + \bar{v}\bar{D}_\theta\right).$$

In Eq. (16), M defines the mean kinetic energy transport terms, E defines the eddy transport terms which represent the Reynolds stress contributions in the azimuthal dimension, P defines the pressure gradient term and D defines the total explicit diffusion term.

Fig. 10 shows a times series of azimuthal mean kinetic energy budget tendencies from both WRF and NUMA after averaging the fields over the eyewall ($\sim$ 10 - 50 km radius) and height ($\sim$ 0.19 - 1.5 km). The largest term is the pressure gradient, which contributes positively to the increase in mean kinetic energy of the vortex shown in Fig. 7. This large positive contribution is from the input heating, which leads to significant integrated warming in the storm core and an associated increase in the radial pressure gradient between the undisturbed outer regions and lowered pressures in the core region.

This larger radial pressure gradient drives strong inflow at low levels, which transports high angular momentum from the outer regions of the storm towards the center, increasing the tangential velocity of the vortex. Large differences between WRF and NUMA are present in the pressure gradient term, especially beyond 2 h with NUMA larger than WRF by $\sim$ 25% on average with a maximum of $\sim$ 40%.

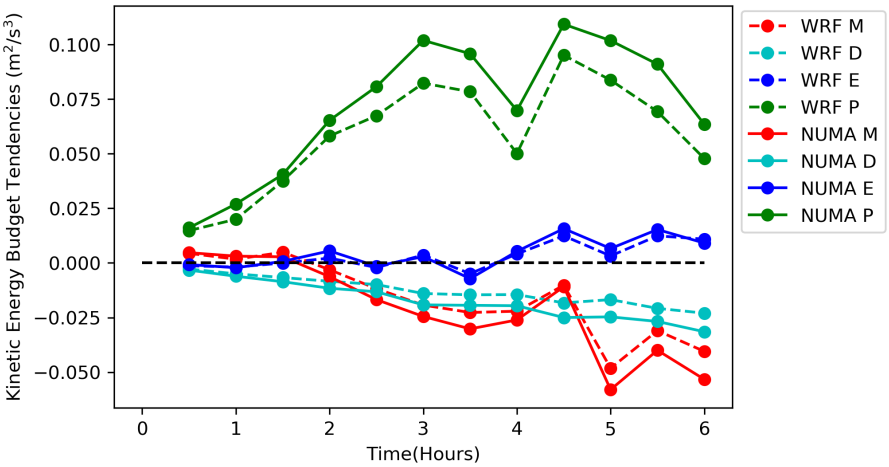

Figure 10: Time series of azimuthal mean kinetic energy budget tendencies from both models after averaging the fields over the eyewall ($\sim$ 10 - 50 km radius) and height ($\sim$ 0.19 - 1.5 km). The black dashed line highlights zero tendency and all other lines are denoted in the key.

The second largest contribution is the mean transport term, which shows largely negative values that increase with time as the mean flow intensifies. The vertical mean transport dominates over the horizontal transport, which is dictated by the heating profile that is maximized near middle levels. Therefore, there is a significant positive flux of kinetic energy out of the lower levels of the vortex, which results in a net sink of energy. However, the differences between WRF and NUMA are much smaller for the mean transport term, relative to the pressure gradient, by a factor of $\sim$ 4.5. The eddy transport term oscillates around zero tendency up until $\sim$ 3.5 h after which a clear positive contribution to the mean kinetic energy is visible. After summing all the budget terms, the eddy transport contributes up to 15 - 40% to the increase in mean KE of the vortex over the 6 h period. When integrating the budget terms over time, the eddy transport contributes 18% to the mean kinetic energy with no notable differences between the models. At these later time periods, the vertical divergence of the vertical tangential momentum flux (the third term in the E contribution in Eq. (16)) has the largest values and provides a positive tendency to the mean kinetic energy in our analysis domain.

For the total explicit diffusion term, the values are very similar before $\sim$ 1 h, but after that time the values from NUMA start to slowly increase relative to WRF with consequential differences at later times into the simulation (NUMA larger than WRF by $\sim$ 36% when averaged from 2 - 6 h). The reason for this is that while the eddy viscosity values are fixed, the velocity gradients in NUMA are larger than WRF (described in the previous section), which produces a larger magnitude in the Laplacian operator. This is not a truly fair comparison of the dynamic cores and a simple diagnostic calculation that accounts for this effect is outlined below.

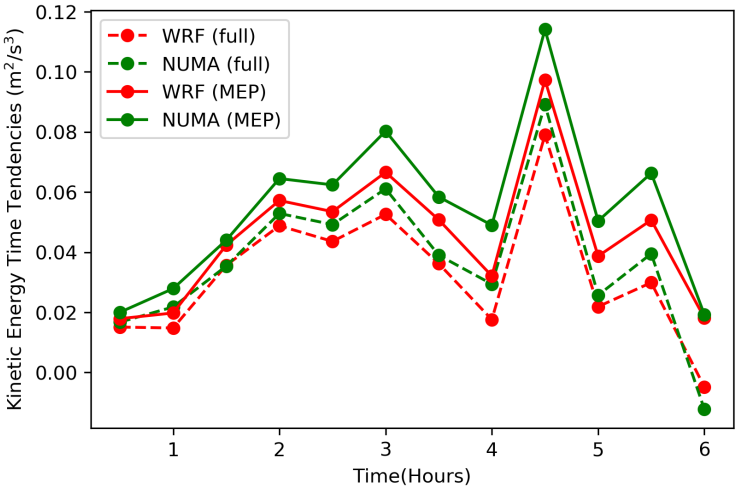

Figure 11: Time series of the summation of terms that control the time tendency of azimuthal mean kinetic energy on the RHS of Eqn (16). The dashed lines represent all terms on the RHS of Eq. (16), while the solid lines include only the M, E and P terms. After summation, the fields are averaged over the eyewall ($\sim$ 10 - 50 km radius) and height ($\sim$ 0.19 - 1.5 km) as is done in Fig. 10.

Fig. 11 shows a times series of the summation of all terms on the RHS of Eq. (16) for WRF and NUMA (dashed lines). This figure represents the slope of the curves displayed in the time series of mean kinetic energy in Fig. 7. Clearly, there is intensification throughout the simulation with the exception of the last output time at 6 h, but note that this weakening is not shown in Fig. 7 because the last output time is right at 6 h. The intensification rate hovers between 0.03 - 0.05 m^2/s^3 over most of the simulation with the exception of a large spike at 4.5 h. After integrating these time series curves with the trapezoidal rule over 6 h with the 30-minute output interval, we find that NUMA has a larger mean (azimuthal mean and averaged over r = 10 - 50 km and z = 0.19 - 1.5 km) kinetic energy than WRF by $\sim$ 8%. However, this difference does not account for the larger explicit diffusion in NUMA mentioned above, which obscures the ability to isolate the effects of implicit numerical dissipation. To correct for this, we re-calculated the integrated mean kinetic energy with the explicit diffusion term (D) removed and we find that NUMA has larger values than WRF by $\sim$ 18%. Note that the same percentage difference would be found if we used the exact same explicit diffusion term from either WRF or NUMA (see Fig. 10) in each model. However, there is a coupled, nonlinear evolution of the fields whereby differences in the explicit diffusion affect the other terms in the mean kinetic energy during the simulations. This is difficult to control, and we do not address this issue here.

In summary, the main differences in the mean vortex intensity between WRF and NUMA is due to the radial pressure gradient contribution to the mean kinetic energy with smaller effects from the transport terms and explicit diffusion. However, even the transport and explicit diffusion terms are controlled, for the most part, by the pressure gradient term because the differences in each model's response to the input heating, via the pressure gradient, results in different velocities even very early (e.g., 1 h) into the simulations (see Fig. 10). Thus, differences in the calculation of the nonlinear advective terms in each model is not a significant source of diffusion and this result is consistent with Guimond et al. (2016). In addition, this result follows from the fact that both WRF

and NUMA utilize high-order discretization of the advective terms and WRF showed no tangible differences when switching from the 5th order to 6th order stencil.

Guimond et al. (2016) also identified the pressure gradient term as the controlling factor in dynamic core comparisons between three different models (including WRF and NUMA) for the same vortex analyzed here. However, Guimond et al. (2016) only considered idealized potential temperature perturbations to the initial state of the model as opposed to the time-dependent, 3-D observational heating used here. Guimond et al. (2016) conducted sensitivity tests with different order time integration schemes and found significant differences in the solutions, which led to the conclusion that the diffusion in WRF was due to the temporal discretization. Similar sensitivity tests were conducted in this work by comparing the control NUMA run (essentially a first-order in time method) to a second-order in time Runge-Kutta method, which is very similar to WRF. These sensitivity tests in NUMA revealed small differences with peak absolute values of ~ 1.5 m/s (not shown) indicating that the temporal discretization is *not* significantly affecting the solutions in either NUMA or WRF. For the spatial discretization of the pressure gradient term, WRF uses second-order finite differences while NUMA is utilizing 5th-order polynomials, which also provides fifth-order accuracy for the pressure gradient evaluation. Given the kinetic energy budgets and sensitivity tests described above, we assess that the low-order spatial approximation of the pressure gradient term in WRF is the source of the significant diffusion in the vortex intensity identified in this paper.

Given the large model differences in the pressure gradient contribution to the mean kinetic energy demonstrated in Fig. 10, it is imperative to examine the full structure of this term to identify any potential localized signals. The components of the horizontal pressure gradient contribution to the kinetic energy in cylindrical coordinates are given as

$$\frac{-u}{\rho}\frac{\partial \hat{p}}{\partial r} \quad \text{and} \quad \frac{-v}{\rho}\frac{\partial \hat{p}}{\partial \theta}$$

where u and v are the radial and tangential wind speed, respectively. Figs. 12 and 13 show horizontal cross sections of these terms, averaged over low-levels (~ 0.19 - 1.5 km), at 4 h and 5 h into the simulations, respectively. In addition, select height-averaged (over the full column) heating inputs to the models leading up to these time periods are also shown in Figs. 12 and 13.

Figs. 12a, 12b show the heating inputs at 3.33 h, 4 h, which represent the heating snapshots leading up to the 4 h mark in the simulations. The 4 h heating has the larger weight in the model results, but there is still some "memory" of the heating from earlier times. The radial component of the pressure term in WRF (Fig. 12c) and NUMA (Fig. 12e) shows an azimuthal wavenumber-2 structure in the eyewall region, which is connected to the input heating structure most closely at 4 h. The heating at 4 h shows localized regions of large positive and negative heating rates (see, for example, the feature to the West of the storm center in Fig. 12b), which are correlated with the positive/negative couplet in the radial pressure term in a similar region. Note that due to the vortex drift to the South-East over time, the heating input and radial pressure term are not exactly aligned. Comparing the radial pressure term from WRF and NUMA shows that NUMA has larger values than WRF, especially in the localized positive regions. This is the reason why the azimuthal average of these fields (see Fig. 10) shows NUMA with much larger values than WRF. *This result indicates that strong, localized heating regions associated with convective bursts are producing a concomitant, enhanced pressure gradient response in NUMA that is driving the differences in the intensification of the vortex.* The reduced, localized pressure gradient values in WRF are due to diffusion from the low-order spatial discretization of this term, as described above.

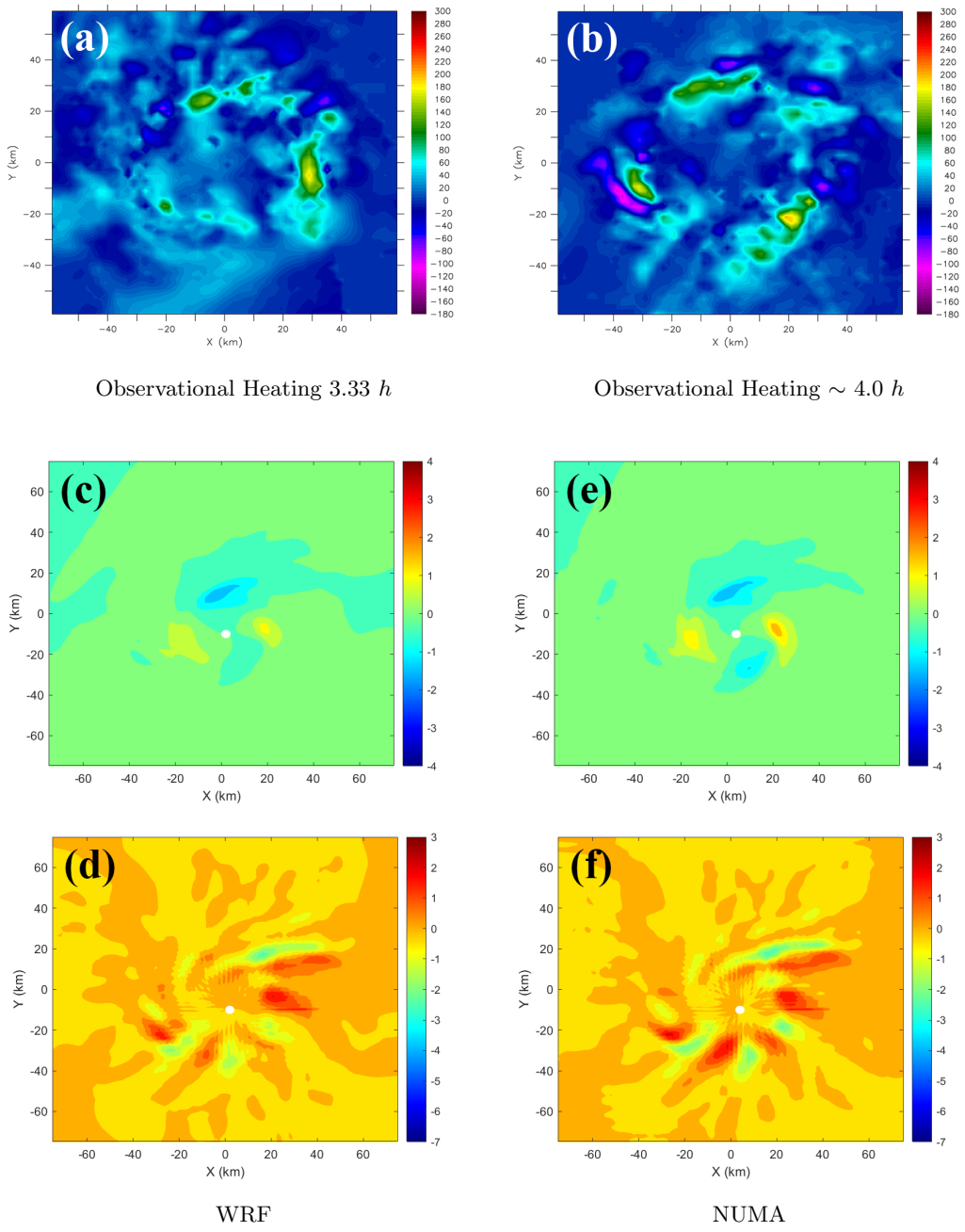

Figure 12: Panels (a) and (b) show the height-averaged, observational heating inputs to the models for time periods 3.33 h and $\sim$ 4 h, respectively. Panels (c) and (d) show the horizontal pressure gradient contributions to kinetic energy in WRF for the radial and tangential components, respectively. Panels (e) and (f) are the same as in (c) and (d), only for NUMA. Panels (c) - (f) are at 4 h into the simulations.

The azimuthal component of the pressure term for this time period in both WRF (Fig. 12d) and NUMA (Fig. 12f) shows a clear azimuthal wave structure with an average wavelength of $\sim$ 20 km and $\sim$ wavenumber-5 structure. These waves are very likely convectively forced vortex Rossby waves (M. T. Montgomery & Enagonio, 1998), but are

not discussed in detail. The anticipated vortex Rossby waves in NUMA have a larger amplitude than those in WRF and this can be seen most clearly to the south of the vortex center.

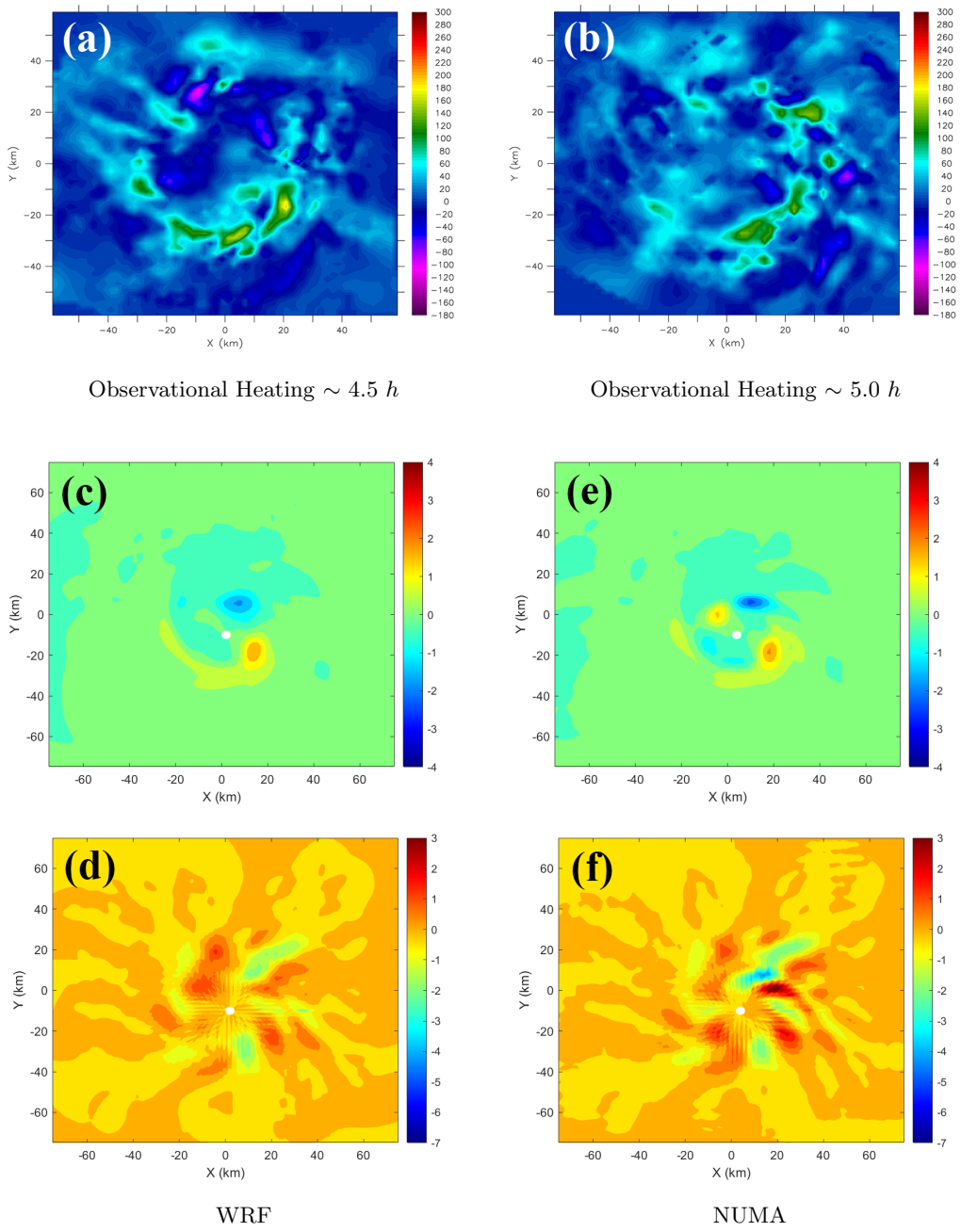

Figure 13: Panels (a) and (b) show the height-averaged, observational heating inputs to the models for time periods $\sim 4.5\ h$ and $\sim 5.0\ h$, respectively. All other panels are the same as in Figure 12, only for 5 h into the simulations.

Fig. 13 shows the same fields as Fig. 12, only at 5 h into the simulations. Similar results to those at 4 h are observed, including larger magnitude, localized positive anomalies in the radial pressure term in NUMA (Fig. 12e) compared to WRF (Fig. 12c) that are connected to the heating snapshots at this time (Figs. 13a and 13b). The azimuthal pressure term also continues to show evidence of vortex Rossby waves with clearly larger amplitude features to the North and East of the vortex center. The heating input at 5 h (Fig. 13b) shows that the majority of the heating is on the eastern side of the vortex with large, localized regions to the north-east of the center, which is consistent with the larger amplitude waves in NUMA.

4 Summary and Conclusions

In this paper, we have studied the computational fluid dynamics of the hurricane rapid intensification (RI) process by considering idealized simulations of the vortex response to time-dependent, 3D latent heating estimates derived from airborne radar measurements collected in the RI of Hurricane Guillermo (1997). Two types of numerical models were considered: a community-based, finite difference and split-explicit model called WRF and an advanced, spectral element and semi-implicit model called NUMA. The models are carefully analyzed and setup to ensure the differences can be isolated to the numerical schemes that comprise the dynamic core. This includes explicit diffusion settings, which are parameterized based on output from a 3D TKE subgrid model experiment.

Prior studies used simple thermal perturbations to the initial conditions to represent the effects of convective heating and found that the WRF model had significant implicit numerical dissipation when compared to advanced research codes, including NUMA (Guimond et al., 2016). The current study also finds significant implicit numerical dissipation in WRF with a reduction in several intensity metrics over a 6 h period: (1) maximum wind speeds in WRF are $\sim$ 12% lower than NUMA when matching the eddy diffusivity values, (2) time-integrated, mean kinetic energy values in WRF are $\sim$ 20% lower than NUMA when accounting for differences in the LaPlacian diffusion operator and (3) peak, localized wind speed differences in WRF are $\sim$ 12 m/s lower than NUMA. Sensitivity studies show, that in order to achieve a similar intensity time series to NUMA, the explicit diffusion in WRF must be reduced drastically, with eddy viscosity values set to 50% of those in NUMA. In the control simulations, the NUMA windspeeds are visibly larger than WRF by roughly 5 m/s when averaged over the eyewall with local regions exceeding 10 m/s. In addition, NUMA's low wind region in the eye is slightly wider than WRF's, resulting in larger velocity gradients (and larger Laplacian diffusion) when accounting for the enhanced values in the eyewall.

To understand the nature of the differences between the models, the azimuthal mean kinetic energy budget was examined. At all time periods in the 6-hour simulation, the pressure gradient force contribution to the kinetic energy is significantly higher in NUMA compared to WRF by $\sim$ 23% in the mean and $\sim$ 40% in the maximum. Examination of the horizontal components of the pressure term reveal that NUMA produces localized pressure gradient anomalies that are larger in magnitude when compared to WRF. These localized regions are tied into the observational heating inputs that contain the presence of convective bursts, which are prevalent during the RI process. In addition, the presence of azimuthal waves in the pressure gradient term are visible in the simulations, likely vortex Rossby waves, with larger amplitudes in NUMA. While the axisymmetric transport of kinetic energy, especially by vertical fluxes, is substantially larger than the asymmetric transport, we find that these eddy processes contribute 15 - 40% at 30-minute output intervals over the 6 h period and $\sim$ 18% when integrating the terms over time.

Sensitivity tests with different time integration schemes in NUMA were conducted to identify the root numerical causes of the model differences. However, employing a second-

order in time scheme, compared to an essentially first-order in time method for the control run, did not produce any notable differences in the NUMA solutions. This is in contrast to the results in Guimond et al. (2016), where higher order time integration schemes produced even more energetic solutions. The reason for the discrepancy is likely due to the nature of the problem: Guimond et al. (2016) analyzed a freely evolving vortex initialized with a perturbation while the present study considered strong, 4-D forcing. Therefore, the significant diffusion in WRF is controlled by a spatial discretization error and this is consistent with the fact that WRF relies on a diffusive, second-order approximation to the pressure gradient force while NUMA utilized a fifth-order accurate approximation.

We do not know which model solution is correct in the absolute sense and numerical convergence studies are ongoing. However, excessive numerical dissipation is not a desired aspect of a modeling system because it reduces the effective resolution of the simulations and can damage the effects of physics-based sub-grid models and observations used to initialize the model in data assimilation practices. The simulations in this paper were for a short time period (6 h) to accommodate the available observational heating and longer-term simulations that have multiple, episodic convective burst events will likely increase the disparity between the two dynamic cores. Furthermore, the positive feedback loop involving moist physics was not operating in these simulations and coupling of the enhanced windspeeds in NUMA to surface fluxes, microphysical heating and pressure responses will likely add additional divergence in the models. Nevertheless, this paper makes an important step forward in an attempt to develop a holistic, thorough investigation of the computational fluid dynamics of the hurricane RI process.

Acknowledgments

We thank NOAA/HRD for collecting and processing the raw radar data used in this paper. The hardware used for the computational studies in this paper is part of the University of Maryland, Baltimore County (UMBC) High Performance Computing Facility (HPCF). HPCF is supported by the U.S. National Science Foundation through the MRI program (grant nos. CNS-0821258, CNS-1228778, and OAC-1726023) and the SCREMS program (grant no. DMS-0821311), with additional substantial support from UMBC. The contributions of M.B. Hasan and S.R. Guimond are partially supported by the NSF under grant AGS-2121366. Additional support for M.B. Hasan was provided by a UMBC Strategic Awards for Research Transitions (START) grant to S.R. Guimond. S. Reddy and F.X. Giraldo were supported by the Office of Naval Research under grant number N0001419WX00721.

The WRF and NUMA output data are available at the following link: `https://figshare.com/projects/The_Effects_of_Numerical_Dissipation_on_Hurricane_Rapid_Intensification_with_Observational_Heating/126469`.

References

Abdi, D., Giraldo, F. X., Constantinescu, E. M., Carr, L. E., Wilcox, L. C., & Warburton, T. C. (2019). Acceleration of the implicit–explicit nonhydrostatic unified model of the atmosphere on manycore processors. *The International Journal of High Performance Computing Applications*, *33*(2), 242-267. Retrieved from `https://doi.org/10.1177/1094342017732395` doi: 10.1177/1094342017732395

Abdi, D., Wilcox, L., Warburton, T., & Giraldo, F. X. (2017). A gpu-accelerated continuous and discontinuous galerkin non-hydrostatic atmospheric model. *The International Journal of High Performance Computing Applications*, *33*(1), 81-109. Retrieved from `https://doi.org/10.1177/1094342017694427` doi:

10.1177/1094342017694427

Blaisdell, G., Spyropoulos, E., & Qin, J. (1996). The effect of the formulation of nonlinear terms on aliasing errors in spectral methods. *Applied Numerical Mathematics*, *21*, 207–219.

Cockburn, B., & Shu, C.-W. (1998). The runge–kutta discontinuous galerkin method for conservation laws v: Multidimensional systems. *Journal of Computational Physics*, *141*(2), 199-224.

DeMaria, M., Franklin, J. L., Onderlinde, M. J., & Kaplan, J. (2021). Operational forecasting of tropical cyclone rapid intensification at the national hurricane center. *Atmosphere*, *12*(6). Retrieved from `https://www.mdpi.com/2073-4433/12/6/683` doi: 10.3390/atmos12060683

DeMaria, M., Sampson, C., Knaff, J., & Musgrave, K. D. (2014). Is tropical cyclone intensity guidance improving. *Bulletin of the American Meteorological Society*, *95*, 387-398.

Emanuel, K. (1986). An air-sea interaction theory for tropical cyclones. Part I: Steady-state maintenance. *JAS*, *43*, 585–604.

Fischer, P. F., & Mullen, J. S. (2001). Filter-based stabilization of spectral element methods. *Comptes Rendus de lÁcadémie des Sciences - Series I - Mathematics*, *332*, 265–270.

Gassner, G. J. (2013). A skew-symmetric discontinuous galerkin spectral element discretization and its relation to sbp-sat finite difference methods. *SIAM Journal on Scientific Computing*, *35*, A1233–A1253.

Gassner, G. J., & Beck, A. D. (2013). On the accuracy of high-order discretizations for underresolved turbulence simulations. *Theor. Comput. Fluid Dyn.*, *27*, 221—237.

Giraldo, F. X. (2020). *An introduction to element-based galerkin methods on tensor-product bases: Analysis, algorithms, and applications.* doi: 10.1007/978-3-030-55069-1

Giraldo, F. X., Kelly, J. F., & Constantinescu, E. M. (2013). Implicit-explicit formulations of a three-dimensional nonhydrostatic unified model of the atmosphere (numa). *SIAM J. Sci. Comput.*, *35*.

Giraldo, F. X., & Restelli, M. (2008). A study of spectral element and discontinuous Galerkin methods for the Navier Stokes equations in nonhydrostatic mesoscale atmospheric modeling: Equation sets and test cases. *Journal of Computational Physics*, *227*(8), 3849-3877. doi: 10.1016/j.jcp.2007.12.009

Giraldo, F. X., Restelli, M., & Läuter, M. (2010). Semi-implicit formulations of the navier–stokes equations: Application to nonhydrostatic atmospheric modeling. *SIAM J. Sci. Comput.*, *32*, 3394-3425.

Guimond, S. R., Bourassa, M., & Reasor, P. (2011). A Latent Heat Retrieval and Its Effects on the Intensity and Structure Change of Hurricane Guillermo (1997). Part I: The Algorithm and Observations. *Journal of The Atmospheric Sciences - J ATMOS SCI*, *68*, 1549-1567. doi: 10.1175/2011JAS3700.1

Guimond, S. R., Heymsfield, G. M., & Turk, F. J. (2010). Multiscale observations of Hurricane Dennis (2005): The effects of hot towers on rapid intensification. *J. Atmos. Sci.*, *67*.

Guimond, S. R., Reisner, J., Marras, S., & Giraldo, F. X. (2016). The impacts of dry dynamic cores on asymmetric hurricane intensification. *Journal of the Atmospheric Sciences*, *73*, 4661 - 4684. doi: 10.1175/JAS-D-16-0055.1

Guimond, S. R., & Reisner, J. M. (2012). A latent heat retrieval and its effects on the intensity and structure change of Hurricane Guillermo (1997). *Part II: Numerical simulations. J. Atmos. Sci.*, *69*.

Hoffman, J., & Frankel, S. (2001). *Numerical methods for engineers and scientists, second edition,.* Taylor & Francis. Retrieved from `https://books.google.com/books?id=VKs7Afjkng4C`

Honein, A. E., & Moin, P. (2004). Higher entropy conservation and numerical stabil-

ity of compressible turbulence simulations. *Journal of Computational Physics*, *201*(2), 531–545. Retrieved from https://www.sciencedirect.com/science/article/pii/S0021999104002414 doi: https://doi.org/10.1016/j.jcp.2004.06.006

Karamanos, G.-S., & Karniadakis, G. (2000). A spectral vanishing viscosity method for large-eddy simulations. *Journal of Computational Physics*, *163*, 22–50.

Kelly, J. F., & Giraldo, F. X. (2012). Continuous and discontinuous Galerkin methods for a scalable three-dimensional nonhydrostatic atmospheric model: limited-area mode [Article]. *Journal of Computational Physics*, *231*(24), 7988-8008. doi: {10.1016/j.jcp.2012.04.042}

Klemp, J., & Wilhelmson, R. (1978). The simulation of three-dimensional convective storm dynamics. *J. Atmos. Sci.*, *35*, 1070-1096. doi: 10.1175/1520-0469(1978)035⟨1070:TSOTDC⟩2.0.CO;2

Knutson, T., Camargo, S., Chan, J., Kerry, E., Chang-Hoi, H., James, K., ... Liguang, W. (2019). Tropical cyclones and climate change assessment: part II. Projected Response to Anthropogenic Warming. *Bull. Am. Meteorol. Soc.*, *101*, E303-E322.

Knutson, T., Sirutis, J., Zhao, M., Tuleya, R., Bender, M., Vecchi, G., ... Chavas, D. (2015). Global projections of intense tropical cyclone activity for the late twenty-first century from dynamical downscaling of downscaling of CMIP5/RCP4.5 scenarios. *J. Climate*, *28*, 7203-7224.

Kravchenko, A., & Moin, P. (1997). On the effect of numerical errors in large eddy simulations of turbulent flows. *Journal of Computational Physics*, *131*(2), 310-322. Retrieved from https://www.sciencedirect.com/science/article/pii/S0021999196955977 doi: https://doi.org/10.1006/jcph.1996.5597

Laprise, R. (1992). The euler equations of motion with hydrostatic pressure as an independent variable. *Monthly Weather Review - MON WEATHER REV*, *120*. doi: 10.1175/1520-0493(1992)120⟨0197:TEEOMW⟩2.0.CO;2

Larsson, J., Lele, S., & Moin, P. (2007). Effect of numerical dissipation on the predicted spectra for compressible turbulence. *Annual research briefs*.

Li, L., & Chakraborty, P. (2020). Slower decay of landfalling hurricanes in a warming world. *Nature*, *587*(7833), 230—234. Retrieved from https://doi.org/10.1038/s41586-020-2867-7 doi: 10.1038/s41586-020-2867-7

Marks, F., & Shay, L. (1998). Landfalling tropical cyclones: Forecast problems and associated research opportunities. *Bulletin of the American Meteorological Society*, *79*, 305-323.

Montgomery, M., Nicholls, M., Cram, T., & Saunders, A. (2006). A vortical hot tower route to tropical cyclogenesis. *Journal of the atmospheric sciences*, *63*(1), 355–386.

Montgomery, M. T., & Enagonio, J. (1998). Tropical cyclogenesis via convectively forced vortex rossby waves in a three-dimensional quasigeostrophic model. *Journal of the Atmospheric Sciences*, *55*(20), 3176 - 3207. Retrieved from https://journals.ametsoc.org/view/journals/atsc/55/20/1520-0469_1998_055_3176_tcvcfv_2.0.co_2.xml doi: 10.1175/1520-0469(1998)055⟨3176:TCVCFV⟩2.0.CO;2

Moura, R., Mengaldo, G., Peiró, J., & Sherwin, S. (2017). On the eddy-resolving capability of high-order discontinuous Galerkin approaches to implicit LES / under-resolved DNS of euler turbulence. *Journal of Computational Physics*, *330*, 615–623. Retrieved from https://www.sciencedirect.com/science/article/pii/S0021999116305642 doi: https://doi.org/10.1016/j.jcp.2016.10.056

Nolan, D. S., & Grasso, L. D. (2003). Nonhydrostatic, three-dimensional perturbations to balanced, hurricane-like vortices. part ii: Symmetric response and nonlinear simulations. *JAS*, *60*(22), 2717–2745.

Persson, P.-O., & Peraire, J. (2006). Sub-cell shock capturing for discontinuous

Galerkin methods. *Proc. of the 44th AIAA Aerospace Sciences Meeting and Exhibit*, *AIAA-2006-112*.

Qiu, J., & Shu, C.-W. (2005). Runge–Kutta Discontinuous Galerkin Method Using WENO Limiters. *SIAM Journal on Scientific Computing*, *26*, 907—929.

Rappaport, E., Franklin, J., Avila, L., Baig, S., Beven, J., Blake, E. S., ... Tribble, A. N. (2009). Advances and challenges at the national hurricane center. *Weather and Forecasting*, *24*, 395-419.

Reasor, P. D., Eastin, M. D., & Gamache, J. F. (2009). Rapidly intensifying Hurricane Guillermo (1997). *Part I: Low-wavenumber structure and evolution. Mon. Wea. Rev.*, *137*.

Rogers, R., Reasor, P., & Lorsolo, S. (2013). Airborne doppler observations of the inner-core structural differences between intensifying and steady-state tropical cyclones. *MWR*, *141*, 2970–2991.

Shapiro, L. J., & Willoughby, H. E. (1982). The response of balanced hurricanes to local sources of heat and momentum. *Journal of Atmospheric Sciences*, *39*(2), 378 - 394. Retrieved from `https://journals.ametsoc.org/view/journals/atsc/39/2/1520-0469_1982_039_0378_trobht_2_0_co_2.xml` doi: 10.1175/1520-0469(1982)039⟨0378:TROBHT⟩2.0.CO;2

Skamarock, W. C., & Klemp, J. B. (2008). A time-split nonhydrostatic atmospheric model for weather research and forecasting applications. *Journal of Computational Physics*, *227*(7), 3465 - 3485. Retrieved from `http://www.sciencedirect.com/science/article/pii/S0021999107000459` (Predicting weather, climate and extreme events) doi: https://doi.org/10.1016/j.jcp.2007.01.037

Skamarock, W. C., Klemp, J. B., Dudhia, J., Gill, O., Liu, Z., Berner, J., ... yu Huang, X. (2021). A description of the advanced research wrf model version 4. *NCAR Technical Notes*. doi: http://dx.doi.org/10.5065/1dfh-6p97

Sroka, S., & Guimond, S. R. (2021). Organized kinetic energy backscatter in the hurricane boundary layer from radar measurements. *Journal of Fluid Mechanics*, *924*, A21. doi: 10.1017/jfm.2021.632

Takemi, T., & Rotunno, R. (2003). The effects of subgrid model mixing and numerical filtering in simulations of mesoscale cloud systems. *Monthly Weather Review*, *131*(9), 2085 - 2101. Retrieved from `https://journals.ametsoc.org/view/journals/mwre/131/9/1520-0493_2003_131_2085_teosmm_2.0.co_2.xml` doi: 10.1175/1520-0493(2003)131⟨2085:TEOSMM⟩2.0.CO;2

Wang, Z. J., Fidkowski, K., Abgrall, R., Bassi, F., Caraeni, D., Cary, A., ... Visbal, M. (2013). High-order cfd methods: current status and perspective. *International Journal for Numerical Methods in Fluids*, *72*, 811–845.

Wicker, L. J., & Skamarock, W. C. (2002). Time-Splitting Methods for Elastic Models Using Forward Time Schemes. *Monthly Weather Review*, *130*(8), 2088-2097. Retrieved from `https://doi.org/10.1175/1520-0493(2002)130<2088:TSMFEM>2.0.CO;2` doi: 10.1175/1520-0493(2002)130⟨2088:TSMFEM⟩2.0.CO;2

Yu, M. L., Giraldo, F. X., Peng, M., & Wang, Z. J. (2015). Localized Artificial Viscosity Stabilization of Discontinuous Galerkin Methods for Nonhydrostatic Mesoscale Atmospheric Modeling. *Monthly Weather Review*, *143*, 4823–4845.

Zhang, X., & Shu, C.-W. (2010). On positivity preserving high order discontinuous galerkin schemes for compressible euler equations on rectangular meshes. *J. Comput. Phys.*, *229*, 8918–8934.